PNAS RESEARCH ARTICLE | PHYSICS

Biotropic liquid crystal phase transformations in cellulose-producing bacterial communities

Andrii Repula[a], Eldho Abraham[a], Vladyslav Cherpak[a], and Ivan I. Smalyukh[a,b,c,1]

Edited by David Weitz, Harvard University, Cambridge, MA; received January 17, 2022; accepted April 29, 2022

Biological functionality is often enabled by a fascinating variety of physical phenomena that emerge from orientational order of building blocks, a defining property of nematic liquid crystals that is also pervasive in nature. Out-of-equilibrium, "living" analogs of these technological materials are found in biological embodiments ranging from myelin sheath of neurons to extracellular matrices of bacterial biofilms and cuticles of beetles. However, physical underpinnings behind manifestations of orientational order in biological systems often remain unexplored. For example, while nematiclike birefringent domains of biofilms are found in many bacterial systems, the physics behind their formation is rarely known. Here, using cellulose-synthesizing *Acetobacter xylinum* bacteria, we reveal how biological activity leads to orientational ordering in fluid and gel analogs of these soft matter systems, both in water and on solid agar, with a topological defect found between the domains. Furthermore, the nutrient feeding direction plays a role like that of rubbing of confining surfaces in conventional liquid crystals, turning polydomain organization within the biofilms into a birefringent monocrystal-like order of both the extracellular matrix and the rod-like bacteria within it. We probe evolution of scalar orientational order parameters of cellulose nanofibers and bacteria associated with fluid-gel and isotropic-nematic transformations, showing how highly ordered active nematic fluids and gels evolve with time during biological-activity-driven, disorder-order transformation. With fluid and soft-gel nematics observed in a certain range of biological activity, this mesophase-exhibiting system is dubbed "biotropic," analogously to thermotropic nematics that exhibit solely orientational order within a temperature range, promising technological and fundamental-science applications.

liquid crystals | nanocellulose | self-assembly | active matter | bacteria

Significance

Upon increasing temperature, melting of solids often occurs as a multi-step process, with mesophases in-between crystalline and fluid phases of matter. Our findings show how natural biological processes can drive transitions in the opposite direction, from disordered fluid to orientationally ordered nematic fluid and solid-like hydrogel states. Using bacteria *Acetobacter xylinum*, which produce cellulose nanofibers to move, our findings introduce an active matter system with the ordering-transition-driving activity, as well as shed light on formation of nematiclike structures in bacterial communities. Naturally forming as birefringent extracellular matrices in biofilms, these bacteria-made nanocellulose fluids and gels can be grown as nematic monodomains and converted to ordered aerogels, of interest for technological uses as thermally superinsulating materials.

Many biological substances, like cholesterol, lipids, proteins, nucleic acids, microtubules, and viruses are known for their liquid crystalline (LC) phase behavior in either pure form or when in aqueous solutions and suspensions (1). The very first documented observations of LCs from well over a century ago utilized substances like derivatives of cholesterol extracted from living organisms (2, 3). Moreover, created within natural processes, LC-like structural organizations in tissues and key components of biological systems, like membranes, tend to endow complex functionality that remains superior to that of man-made materials (4, 5). Recognizing these important roles of LC-like organization, a biologist, D. Dervichian, once wrote "Liquid crystals stand between the isotropic liquid phase and the strongly organized state. Life stands between complete disorder, which is death and complete rigidity which is death again" (6). Understanding and recreating these LC-like nature's elegant designs can revolutionize our ability of cost-effective mass-production of "living" materials and devices with attractive properties like low-cost, green manufacturing, self-healing and regeneration. However, how nature creates LC-like structures within out-of-equilibrium processes remains poorly understood despite of their diverse and ubiquitous observations (1–6).

A particularly interesting form of a natural LC-like organization relates to bacterial biofilms, where birefringent domains of extracellular matrix and orientationally ordered bacteria have been reported for many microbiological systems (7–21). For example, *Acetobacter xylinum* (*A. xylinum*) bacteria biosynthesize cellulose filaments which can be organized in an orderly manner at the micrometer scales while exhibiting randomly aligned domains on larger scales within the three-dimensional (3D) reticulated biofilm (22–26). Limitations in controlling morphology and order within such biofilms hinder potential applications of bacterial cellulose-based materials (15–19). Here, we elucidate how a natural biological process leads to a spontaneous LC order of both cellulose nanofibers, which form an anisotropic extracellular matrix with strongly pronounced birefringence, and rod-like *A. xylinum* bacteria within a mesostructured active nematic system that can take both polydomain and monodomain structural forms. We probe orientationally ordered active nematic states in both aqueous environment and atop of

Author affiliations: [a]Department of Physics and Chemical Physics Program, University of Colorado, Boulder, CO 80309; [b]Chirality Research Center, Hiroshima University, Higashi Hiroshima, Hiroshima 739-8526, Japan; and [c]Renewable and Sustainable Energy Institute, National Renewable Energy Laboratory and University of Colorado, Boulder, CO 80309

Author contributions: I.I.S. designed research; A.R., E.A., and V.C. performed research; A.R. analyzed data; and A.R. and I.I.S. wrote the paper.

The authors declare no competing interest.

This article is a PNAS Direct Submission.

[1]To whom correspondence may be addressed. Email: ivan.smalyukh@colorado.edu.

This article contains supporting information online at http://www.pnas.org/lookup/suppl/doi:10.1073/pnas.2200930119/-/DCSupplemental.

Published June 7, 2022.

solid agar surfaces. Using video-microscopy within different optical imaging modalities, we document the spontaneous emergence of nematic ordering in the course of biological activity. We find that directional feedings (and separately synthesized nematic hosts of colloidal nanocellulose used in our test experiments) break symmetry and lead to monodomain-like active nematic organizations, which we then use to quantitatively probe how orientational order of cellulose nanofibers and bacteria evolves with time. Holographic laser tweezers reveal onsets and details of formation of hydrogels with anisotropic networks of nanofibers. Characterization of distinct types of motions associated with *A. xylinum*'s nanocellulose production, as well as the estimation of order parameters (27, 28) in nematic and isotropic fluids and gels, reveals an active nematic system with disorder-to-order transformations driven by biological activity. Further, we show that such bacteria-made hydrogels can be readily converted to anisotropic aerogels and discuss how they may find diverse technological uses ranging from thermal insulation to scaffolding of biological tissue within LC-like matrices.

Results

Pervasive Nematic Order in Bacterial Communities. When *A. xylinum* cells are placed into a nutrition-containing medium (23, 25, 29), they synthesize cellulose subfibrils of diameter 2–4 nm ejected from an array of enzymatic macromolecular sites along the bacterium length (18, 22) (Fig. 1*A*). The subfibrils are made of aligned, crystallized cellulose polymer chains (18), which further self-assemble into fibers of 20–100 nm in diameter (18, 22) via hydrogen bonding between hydroxyl surface groups. While the cellulose polymerization takes place on the synthetic sites along the cell, forces stemming from the cellulose extrusion propel the bacterium, tracing the swimming direction with the fiber (22, 30) (Fig. 1 *B* and *C*). Under natural conditions, the cellulose fibers produced by *A. xylinum* form pellicles interlinked by hydrogen bonds (22), which in turn assemble into nematic hydrogels with polydomain orientational order (Fig. 1 *D* and *E* and SI Appendix, Fig. S1). The nematic order is a pervasive feature of the cellulose-synthesizing bacterial communities. We find it in pellicles formed both under natural conditions and in glass cells or microfluidic channels with nutrient-enriched water medium (Fig. 1 and *SI Appendix*, Fig. S1), as well as atop of solid agar surfaces (Fig. 2). The quasi-two-dimensional nature of nematic domains formed on agar surfaces reveals fascinating structural organizations with defects of integer and half-integer winding numbers, which quantify how many times the bacteria/ cellulose and nematic director $\mathbf{n}(r)$ rotate by 360° as one circumnavigates such a defect's core once (Fig. 2). Each circular island of a bacterial community has a +1 defect (the positive sign here refers to the director rotation following the counterclockwise direction of defect circumnavigation) with concentric structure of $\mathbf{n}(r)$ and with the density of cells gradually increasing when going from the domain's periphery toward its center (Fig. 2 *A*–*E*). The circular domain's edges effectively impose tangential boundary conditions for $\mathbf{n}(r)$ on its periphery (Fig. 2 *E* and *F*). The outgrowth of new adjacent regions of the bacterial colony on solid agar surfaces takes place through the formation and unbinding of half-integer defects of opposite signs (Fig. 2 *G* and *H*), which then preserves the orientation of $\mathbf{n}(r)$ tangent to the enlarged

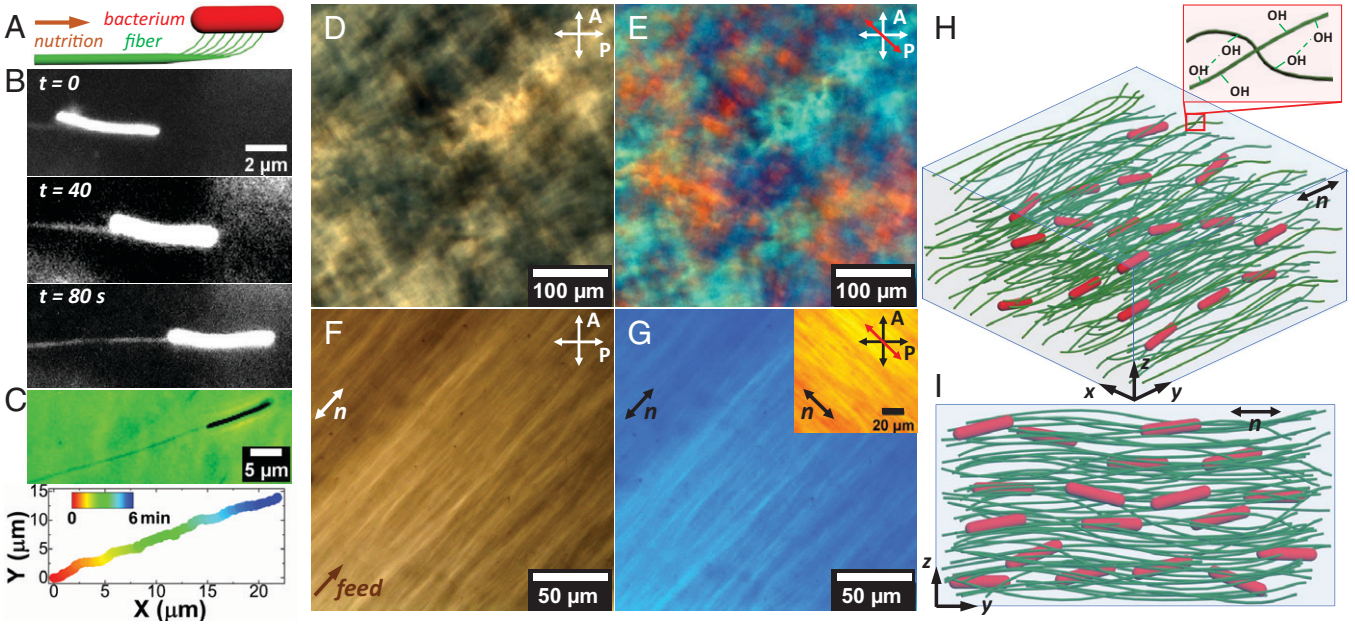

Fig. 1. Bacterial cellulose biosynthesis and its biodirected assembly into the nematic hydrogel. (*A*) Schematics of the bacterial cellulose fiber production by *A. xylinum*, which swims along the direction of nutrition supply. A single filament consists of the elementary subfibrils which are extruded from the bacterium synthetic sites and then assemble into the fiber via the hydrogen bonding (22). (*B*) Successive dark-field microscopy images showing a self-propelled cell as it produces a cellulose nanofilament visible due to light scattering. (*C*) Phase contrast microscopy image showing the cell (*Top*) and its color-time-coded trajectory (*Bottom*), which the bacterium underwent while synthesizing the cellulose filament; the color-time coding scheme is shown in the inset. (*D*–*G*) Polarizing microscopy textures of the polydomain (*D* and *E*), and monodomain (*F* and *G*) cellulose nematic hydrogels produced by the conventional and unidirectional supply of cells with nutrients, respectively (*SI Appendix*, Fig. S1). (*D* and *F*) show the images obtained between the crossed polarizers, whereas images in (*E*) and (*G*) are taken with the additional retardation plate introduced to the optical path and oriented with the slow axis (red double arrow) at 45° to both polarizers (white or black double arrows). Blue-color (*G*) and yellow-color (*Inset* of *G*) textures demonstrate the optical shift when the slow axis is, respectively, perpendicular and parallel to the monodomain nematic director **n**. (*H*) 3D schematics and (*I*) the cross-section of the monodomain nematic hydrogel formed by the cellulose (green filaments) which was synthesized by the bacteria (red rods) when guided by the unidirectional nutrition supply. (*Inset* of *H*) illustrates the internanofiber hydrogen bonding which promotes the cross-linking of the nanocellulose into a hydrogel network. Optical images and data for all figures are acquired from the samples with no CMC additives, unless mentioned otherwise.

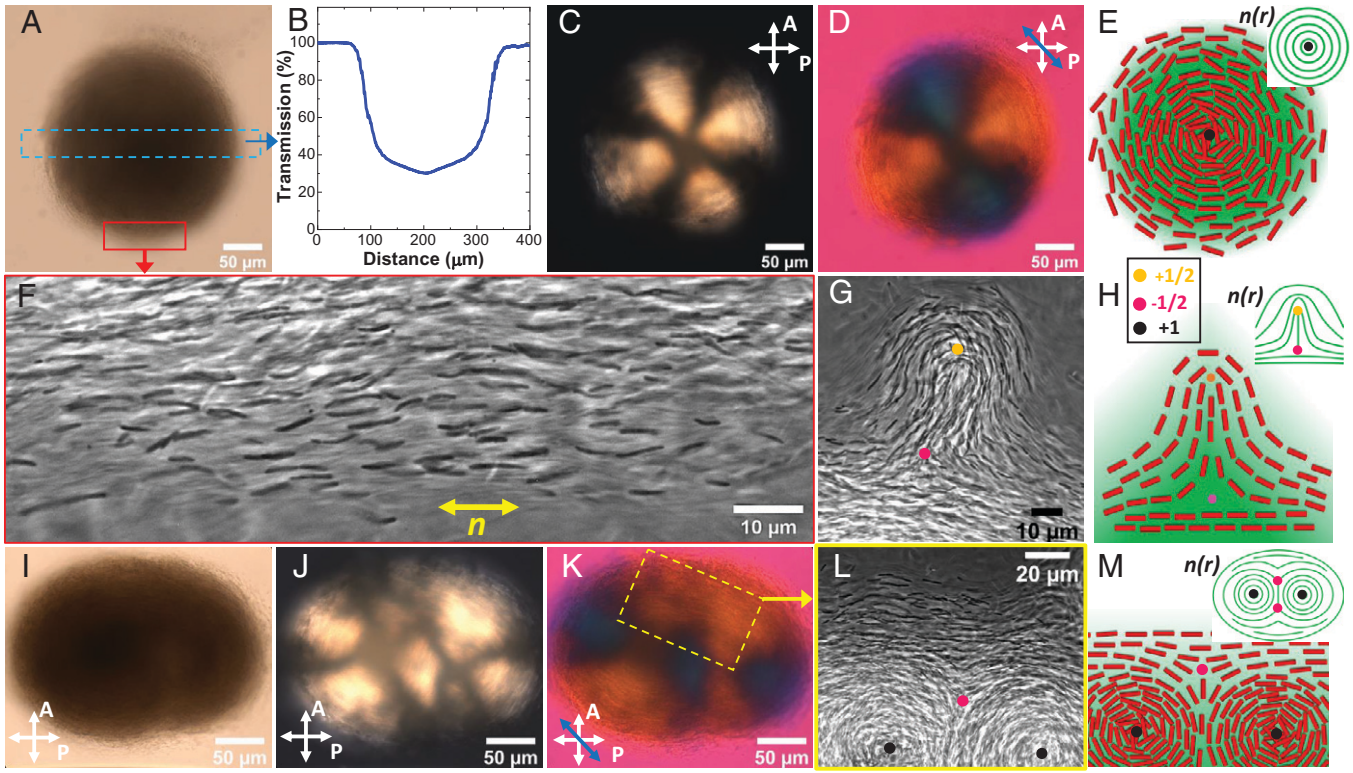

Fig. 2. *A. xylinum* colony grown on the solidified agar surface with cells generating a matrix of cellulose fibers. (*A*) Bright field microscopy image of an isolated colony. (*B*) Light transmission measured along the region marked by a blue dashed rectangle in (*A*), passing through the colony's center. Optical image obtained between the cross polarizers shown by white double arrows (*C*) and with additionally inserted retardation plate, with its slow axis shown by the blue double arrow (*D*). Birefringent texture in (*C*) and (*D*) reveals +1 topological defect in the center of the colony. (*E*) Schematic representing the cross-section through the colony at a distance ~1 μm from the agar surface, where the red rods illustrate the bacterial cells, green gradient color depicts the fiber density deduced from (*B*), and the black filled circle shows the +1 defect. (*Inset* of *E*) shows the nematic director field **n**(r) in the isolated colony. (*F*) Zoomed-in phase contrast microscopy image of *A. xylinum* colony's edge (in a region marked by the red box in *A*) at single-cell resolution which shows bacterial alignment along the director **n**. (*G*) Phase contrast image demonstrating the emergence of +1/2 and −1/2 topological defects during the domain outgrowth at the colony's edge. (*H*) Schematics illustrating the +1/2 and −1/2 defect pair within the orderly bacterial orientations and (*Inset* of *H*) the corresponding director field **n**(r). Biofilm consisting of two merged colonies with +1 defects in their centers captured with (*I*) bright field, (*J*) between the crossed polarized without, and (*K*) with additionally inserted 530 nm phase retardation plate, where the blue double arrow depicts the plate's slow axis. (*L*) Phase contrast image revealing the appearance of −1/2 defect as a result of two colonies merging. (*M*) Schematics illustrating the two +1 and the two −1/2 defects in the patterns of rod-like bacterial orientations and (*Inset* of *M*) corresponding to director field **n**(**r**).

bacterial community domain's edge. The larger communities (in some cases formed from merging of circular islands) tend to feature multiple integer and half-integer defects with their winding numbers adding to +1, with an example shown in Fig. 2 *I–M*. Such behavior vividly resembles the topology and structure of circular islands in nonbiological soft matter systems like islands of thin nematic films and molecular monolayers with in-plane orientational order (31).

While active nematic systems commonly tend to host defects and constantly evolving patterns of multidomain director field, interestingly, we find that monodomain active nematic hydrogels (Fig. 1 *F–I*) can also emerge in our system when the cell communities grow in presence of a unidirectional nutrition supply. The striking difference between the polydomain and monodomain nematic hydrogels is revealed with polarizing optical microscopy (Figs. 1 and 2). By controllably supplying nutrition (*SI Appendix*, Fig. S1), consecutive unidirectional feedings yield a monodomain nematic gel with long-range-aligned cellulose fibers interlinked into a network by hydrogen bonding (Fig. 1*H*). Originating from the symmetry breaking caused by the nutrition supply, rod-like bacterial motion and cellulose production define the orientation of the monodomain nematic director **n** to point along the feeding direction, albeit a few randomly oriented fibers can still exist outside of the well-defined nematic domains, near confining walls. Much like surface rubbing and external fields can enable monodomain nematic LCs in applications like displays, unidirectional feeding prompts monodomains of the active nematic discussed here, albeit it is important to stress that the nematic ordering itself emerges even without such special type of directional nutrient supply (Figs. 1 and 2).

From Chemotaxis to Active Nematics. To probe the nematic order and cross-linked hydrogel networks, we conducted optical microscopy observations in the dark field and phase contrast modes at the single bacterium and fiber levels, respectively (Fig. 3). *A. xylinum* number density ρ (Fig. 3 *A* and *B*) as well as orientational order parameters (Fig. 3 *C* and *D*) of bacteria S_b and fibers S_f [defined as $S_{b,f} = 1/2 < 3cos^2(\theta_{b,f}) - 1 >$, where $\theta_{b,f}$ is the angle between the bacteria's or fiber's long axis and **n** (32)] were quantified 12 h after each feeding η. The feedings in these experiments were performed with 24 h periodicity (24) while starting from the initial injection of diluted cell dispersions ($\eta = 0$ at time $t = 0$) into the microfluidic channel. We observed the monotonic growth of cell number density ρ with time and its apparent saturation after around 5 d (Fig. 3 *A* and *B*). After the injection ($\eta = 0$) and before the first feeding ($\eta = 1$), the weak cell and fiber order are detected (Fig. 3 *C* and *D*) and can be explained by the combination of biological activity and symmetry breaking caused by the initial injection of the bacterial dispersion with nutrients into the microfluidic

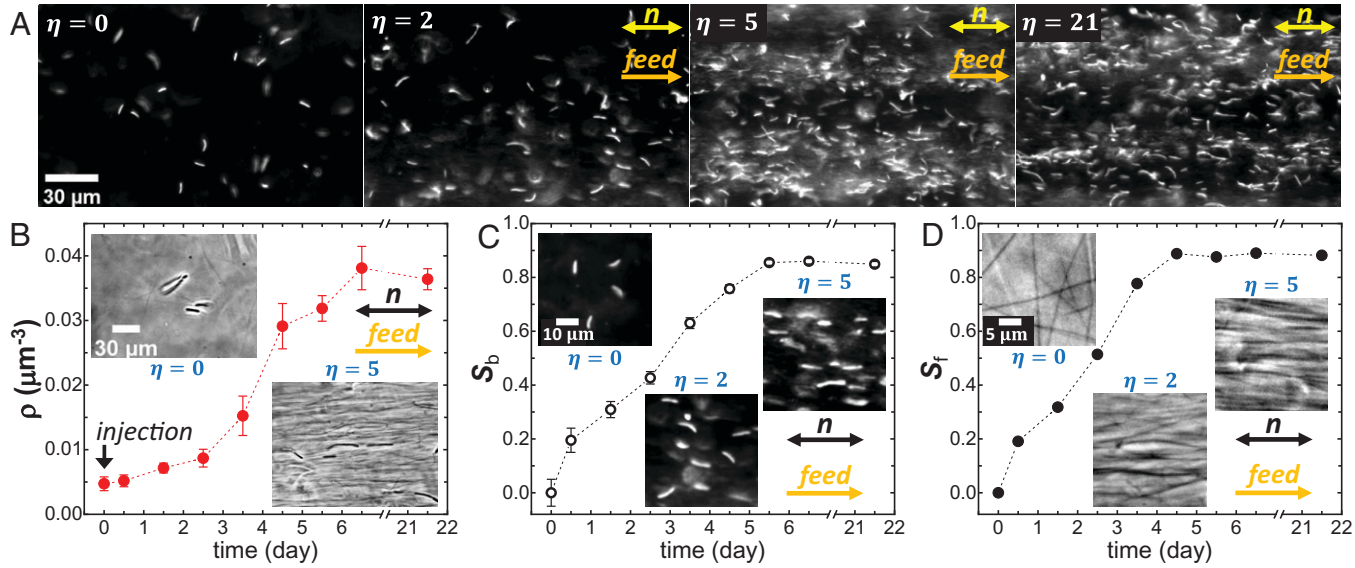

Fig. 3. Bacterial cell density and orientational order parameters versus time and the feeding number η. (*A*) Dark field microscopy images showing the time evolution of the bacterial number density and their alignment with time and as periodical feeding occurs; η is marked on images. (*B*) Injection ($\eta = 0$) of the highly diluted bacteria with few fibers into the microfluidic channel is done at the time $t = 0$. The feeding (injection of the fresh nutrition medium) is performed with 1-d (24 h) intervals, whereas ρ is measured in 12 h after each feeding by analyzing the corresponding optical micrographs. The mean value and the error bars of estimating ρ are based on counting cells on images taken at different focal depths. (*Inset* of *B*) Phase contrast images demonstrating the change of cellulose fiber concentration and orientation as bacteria density increases. (*C* and *D*) The order parameters of bacteria S_b (*C*) and cellulose fibers S_f (*D*) which are measured in the course of days using the distribution functions of particle orientations. S_b *and* S_f are measured in 12 h after each feeding by analyzing the corresponding optical microscopy images *Insets*: zoomed-in dark-field snapshots of bacteria (*C*) and phase contrast images of the cellulose fibers (*D*) indicating the increased orientational order in the hydrogel network with each consecutive feeding. There was no detectable order of cells or fibers at the time of injection, but weak order emerged within 12 h after injection and before the first feeding, when nutrients were available only from the initial composition of the host medium. The orientational order parameters saturate after 5 d. Error bars for S_b and S_f are determined by the accuracy of angular measurements with optical microscopy and are not shown if smaller than the symbols (see *Materials and Methods*).

channel, which we will probe in detail below. As time progresses in the course of days, both the bacteria and fibers feature the increased ordering characterized by $S_b \sim S_f \sim 0.9$, even though their temporal evolution is different. The monodomain nematic director **n** is parallel to the nutrition supply direction (Fig. 3). S_f appears to saturate faster than S_b, which likely is because the cellulose fibers are much longer than the bacterial cells. While such processes also take place in the polydomain samples under natural conditions, the monodomain configurations of our samples allows for in vivo observing the biotropic isotropic-to-nematic phase transition, where the orientational order parameters of both the bacterial cells and the extracellular network grow with time during biological activity (Fig. 4 *A*–*L*).

An important question is how exactly the polar in nature of feeding directionality couples to the observed nonpolar orientational order in the active nematic gels observed forming over time. Fig. 4 *A*–*E* and the Movie S1 directly reveal the bacterial response to the feeding, which prompts the cells to move toward the injected food. The chemotaxis of *A. xylinum* bacteria (33) in this medium with inhomogeneous nutrient distributions occurs in a polar fashion toward the nutrition-enriched regions (Fig. 4 *A*–*E* and Movie S1), consistent with previous observations (33). Within the nutrient-depleted medium, this process breaks the symmetry and results in the production of aligned fibers directed toward the food source (Fig. 4 *A*–*E*). As the food injection breaks the symmetry and increases nutrient concentration on one end of the channel, the bacterial swimming toward the higher nutrient concentration is initially polar in nature, yielding fibers directed to the nutrient enriched regions (Fig. 4 *A*–*E* and Movie S1). With time, the nutrition concentration in the sample equilibrates as the time needed for nutrients to diffuse across the channel's half-width is $t \sim d^2/D_{glucose} \sim (0.5\ cm)^2/10^{-5}\ cm^2\ s^{-1} \sim 10^6\ s \sim 3$ h, shorter than the interfeeding time gap. Therefore, eventually the cells propel in the directions parallel and antiparallel to the feeding direction due to collective interaction of cells with the aligned fibers. Within the overall process, bacterial trajectories initially point in different directions while the cells consume nutrients available from the initial nutrient-enriched medium (Fig. 4*M*), but with time become overall aligned along **n** after the directional feeding (Fig. 4 *N* and *O*). Interestingly, individual cell motions in the viscous nematic gel medium often resemble spirals of different diameters (26), including nearly straight lines in a limiting case. Complex motions of bacteria within such gels also include rotations around their axes, when prompted by the fiber twisting to relieve the strain induced by interactions with other fibers produced by different bacteria (30) (Movie S2). The progression from random motions of active *A. xylinum* (Fig. 4*F*) traced by disordered fibers (Fig. 4*G*) toward an aligned state of both bacteria and fibers (Fig. 4 *H* and *I*) shows both the spontaneous emergence of an active nematic LC and the means of controlling it with directed feeding. The tendency of *A. xylinum* to swim toward the nutrient supply (Fig. 4 *A*–*C* and Movie S1) provides a mechanism of orienting **n** in a desired direction, much like this is done with defining surface anchoring conditions and via coupling to external fields in conventional LCs. As the nutrition concentration equilibrates with time after each feeding, the cell propulsion changes from polar (Fig. 4*D*) to nonpolar nematic (Fig. 4 *N* and *O* and Movie S3) but still collinear with the direction of feeding due to collective interaction of cells with the aligned fibers. After several consecutive feedings, the fraction of active bacteria within dense monodomain nematic LCs starts decreasing, although some bacteria persist their motions while following **n** (Fig. 4*L* and Movie S2). This reduced activity could be due to both nutrient accessibility and the dense hydrogel network hindering motions.

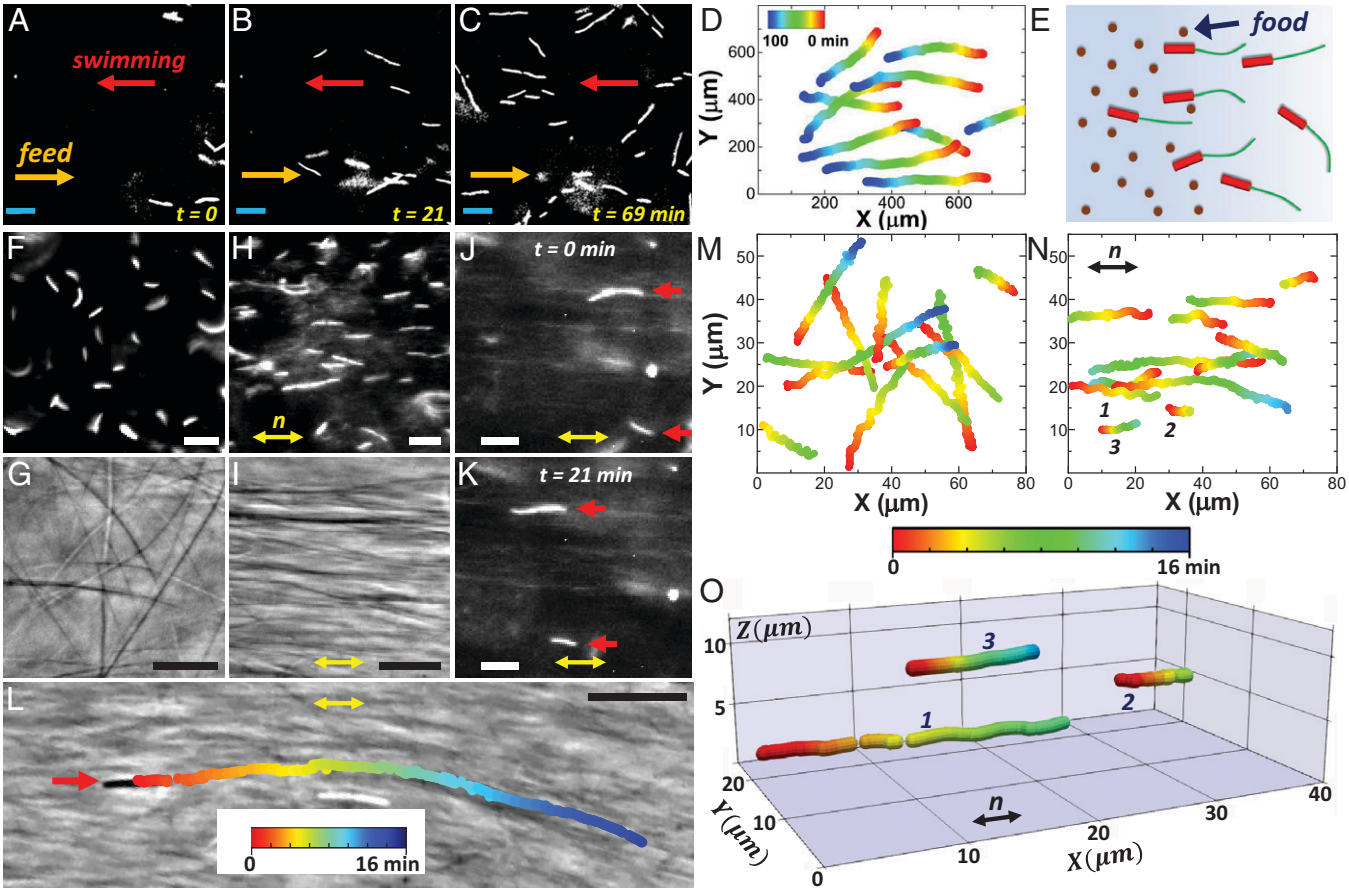

Fig. 4. Evolution of structure and motility of the bacterial community. (*A*–*C*) Successive dark field microscopy images showing the bacterial polar swimming toward the nutrients, with injection direction marked by an orange arrow. (*D*) Time-colored bacteria trajectories within ∼2 h after nutrient refreshment, showing the predominantly polar cell propulsion. (*E*) Schematic illustrating the polar swimming of cells toward the nutrient-enriched regions, accompanied by production of aligned fibers after food refreshment. (*F*) Dark-field and (*G*) phase contrast microscopy images showing the random orientation of the cells and cellulose fibers, respectively, soon after injection of cells into the microfluidic channel ($\eta = 0$). (*H* and *I*) Typical snapshots illustrating the aligned bacteria (*H*) and filaments (*I*) in the nematic state ($\eta = 4$), where the director **n** is denoted by the yellow double arrow, indicating an average orientation of both fibers and bacteria. (*J* and *K*) Successive dark-field images of the active nematic monodomain hydrogel, indicating the displacement of the active swimmers (pointed by red arrows) along **n** and the nutrition supply direction. (*L*) Overlay of the phase contrast image and trajectory of a tracked bacterium (pointed by red arrow), which swims through the nematic hydrogel network and follows the local director field. Scale bars: 10 μm. (*M* and *N*) A collection of the typical motile bacteria trajectories in the disordered (*M*) and nematic (*N*) hydrogels represented according to the time-color scale shown in the *Inset* of (*M*)–(*O*). All trajectories are obtained ∼12 h after corresponding feedings and nutrient diffusion thought the sample. Bacterial cell trajectories numbered by *1*, *2*, and *3* in (*N*) are used for the 3D representation of particle positions over time in the nematic state (*O*).

Controlling and Probing Active Nematic Gel Networks. To control the cellulose fibers' self-assembly and gelation tendencies, we have explored the effect of adding carboxymethyl cellulose (CMC) on our active nematic LCs. The CMC is known to inhibit coassembly of the secreted elementary subfibrils into fibers and gel networks (Fig. 1*A*) due to carboxymethyl-group-related electrostatic repulsion upon their surface attachment (34). This surface modification of nanocellulose with CMCs reduces the number density of hydrogen bonds and the ensuing cross-linking of fibers. We have found that the addition of CMC (at 15 g/L) into the nutrition medium boosts the average cell velocities from 2.2 μm/min to 3.8 μm/min in disordered hydrogels, and from 1.4 μm/min up to 3.8 μm/min in the dense nematic gels (34) (*SI Appendix*, Fig. S2 and Table S1). This finding can be attributed to lower density of cross-links within the CMC-modified active nematic gels.

We have further probed local structure of the monodomain nematic hydrogel using a microrheological approach based on the noncontact optical manipulations with laser tweezers. Isolated *A. xylinum* cells not synthesizing cellulose, of typical length 5–7 μm, could be robustly trapped and manipulated using a holographic optical tweezer system operating at the wavelength of $\lambda = 1{,}064$ nm (35). A rod-like bacterium tends to align with its longitudinal axis along the laser beam (Fig. 5*A* and Movie S4), orienting orthogonally to the feeding direction in our experimental geometry. The laser-guided translations of *A. xylinum* cells within the nematic hydrogel have been compared to that in the isotropic fluid (pure nutrition-containing aqueous medium) (Fig. 5). In the latter case, the uninhibited cell manipulation is evidenced by translational motions and robust arranging of the cells into arbitrary predesigned patterns (Fig. 5 *B*–*D*), with the trajectories of a trapped bacterium precisely controlled by steering the laser beam with the help of software (Fig. 5*E*). As the laser trap draws a preprogrammed geometrical figure, the trapped bacterium closely follows the focused beam's path (Movie S4). Such optical manipulation is markedly different within the monodomain nematic hydrogels. Anisotropic intercrosslinked nature of the aligned cellulose fibers imposes strong constrains on the laser-guided bacterium displacement. When translated parallel to the nematic director **n** (Fig. 5*F*), the bacterium follows the laser trap while retaining its orientation along the beam axis. When translated orthogonally to **n** (Fig. 5*G*), the laser-trapped cell orientation often tilts and becomes nearly in-plane to bypass cross-linked fibers acting as the physical barriers (Movie S5). This observation

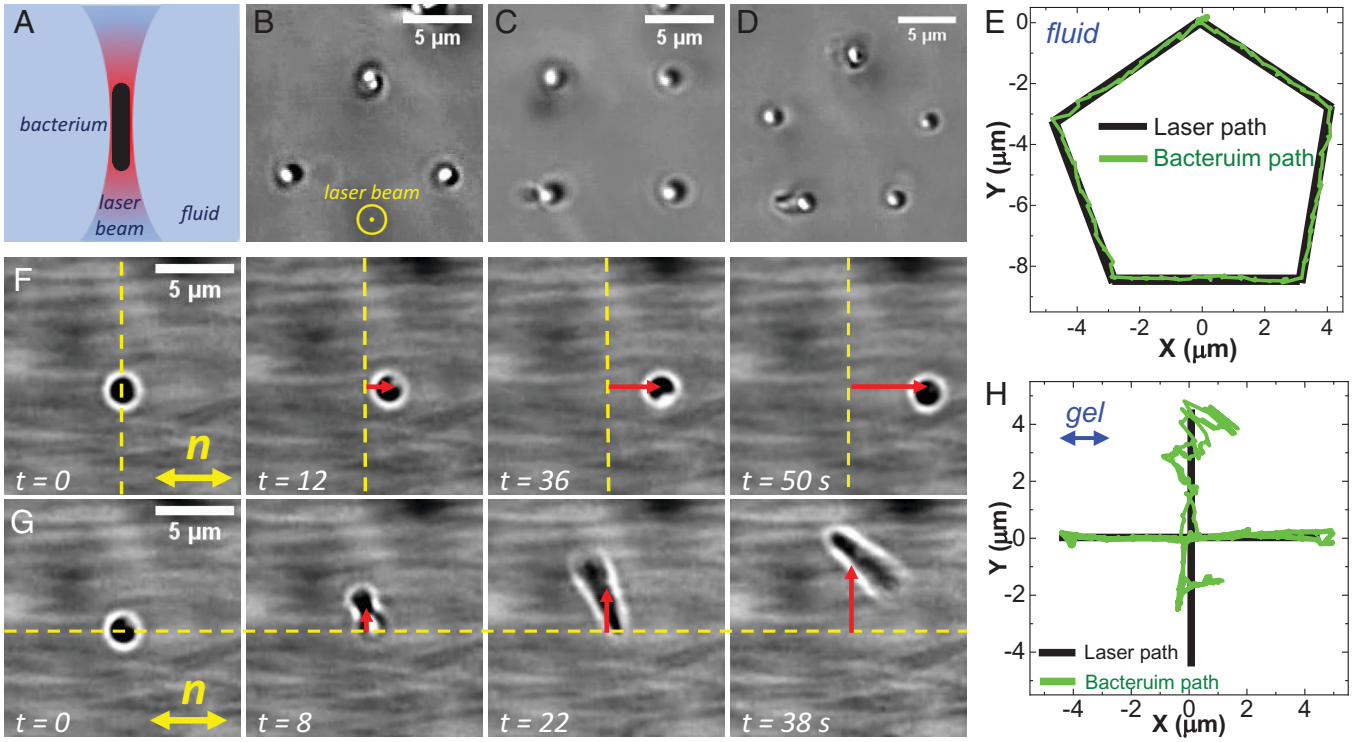

Fig. 5. Microrheological study of the nematic hydrogel structure by manipulating a bacterium with optical tweezers. (*A*) Schematic illustrating that a rod-like cell in the optical trap tends to align along the laser beam. (*B–D*) Bright-field optical images demonstrating the directed assembly of the trapped bacteria into the arbitrary patterns. (*E*) Bacterial cell displacement in the isotropic fluid controlled by the preprogrammed path of the optical trap. (*F*) Successive snapshots showing the bacterium translated parallel to **n** (yellow double arrow) without changing its orientation. (*G*) The cell, which moves perpendicularly to **n**, experiences both the deflection from orientation along the trapping beam and deviation from the trap trajectory. This finding indicates the presence of stiff cellulose fibers causing obstacles along the bacterium trajectory. The red arrows illustrate the particle displacements from the initial positions. (*H*) The overlay of the optical trap path and the respective cell trajectory in a nematic hydrogel, showing a nearly undistorted particle trajectory along **n**, whereas the trace perpendicular to the fibers is strongly affected by the 3D cellulose network. All optical images correspond to the samples with the CMC additive at c_{CMC} = 1.5% by volume.

markedly differs from nearly unperturbed laser-guided cell displacement along **n** and aligned cellulose fibers of the nematic gel (Fig. 5*H*). Video-microscopy of laser-guided translations of *A. xylinum* reveals occasional "bumps" with drifts of bacterial orientation and position relative to the beam center (Movie S6). The CMC addition, which hinders hydrogen bonding of individual fibers, somewhat eases the cell manipulation parallel to **n**. The typical distance between the bumps is 2–3 μm in nematic gels without CMC and 6–8 μm in gels with CMC, revealing the corresponding distances between the fiber network's nodes associated with hydrogen bonding.

Interaction of Cellulose-Synthesizing Bacteria with Orientationally Ordered Cellulose Nanofibers. Directed by the nutrition supply as described above, the unidirectional propulsion of bacteria and the ensuing biosynthesis of cellulose by active *A. xylinum* cells prompts symmetry breaking and biotropic disorder-to-order, isotropic-to-nematic phase transition. This active nematic differs from dispersions of bacteria in preexisting nematic LCs studied previously (8, 36–39), but an important related question is how the cellulose fibers with certain orientations may influence the subsequent motion of bacteria and further production of nanofibers, especially when they form an orientationally ordered state. To address it, one can also disperse the active *A. xylinum* cells into a preexisting colloidal nematic LC host fluid formed by electrostatically stabilized oxidized cellulose nanofibers (OCNs) with 5-nm diameters and 1,000 nm length, which are oxidized by the 2,2,6,6-tetramethylpiperidine-1-oxyl radical (40). In this case, we find that the cell propulsion and the ensuing new fiber cultivation occur parallel to the local director of the LC host medium with added nutrients (Fig. 6 *A*–*C*). Bacterial cellulose fibers biosynthesized within the OCN matrix (Fig. 6*A*) tend to adopt spiral shapes associated with the wavy motility pattern of *A. xylinum* discussed above (Movie S7). The strongly pronounced spiral trajectories and fiber shapes are related to the high host medium's viscosity that precludes fast shape relaxation and freezes the as-secreted fiber shapes upon additional cross-linking due to hydrogen bonds. At the typical used concentration of OCNs 0.7% by mass, nematic domains of the LC host fluid have typical dimensions of several hundreds of microns, with the bacteria swimming roughly along the local OCN LC director (Fig. 6*D*) at velocities of 0.9 μm/min (*SI Appendix*, Table S1). Since the fiber synthesis occurs on the rod-like bacterial cell's side (Fig. 1*A*) and since both the synthesized nanofibers and bacterium tend to orient along the director of the OCN-based nematic host, the process of fiber synthesis inside of such a host medium results in the fiber spiral or its wavy shape. The viscosity of the OCN colloidal dispersion is higher as compared to that of the conventional nutrition medium, thus it also prevents the prompt fiber's shape relaxation, which freezes as-synthesized, retaining the wavy form upon hydrogen-bonding between some of the fibers occurs. The ensuing wavy fibers within the nematic domains of the host medium roughly follow the local director **n** orientation (Fig. 6*E*), with the geometric parameters of fiber conformations dependent on the OCN concentration and various preparation conditions. Overall, our findings show that the bacteria move and new cellulose fibers are produced while oriented roughly along the director of the nematic host, revealing interactions between preexisting oriented fibers and both the bacterial motion directions and the newly synthesized fibers.

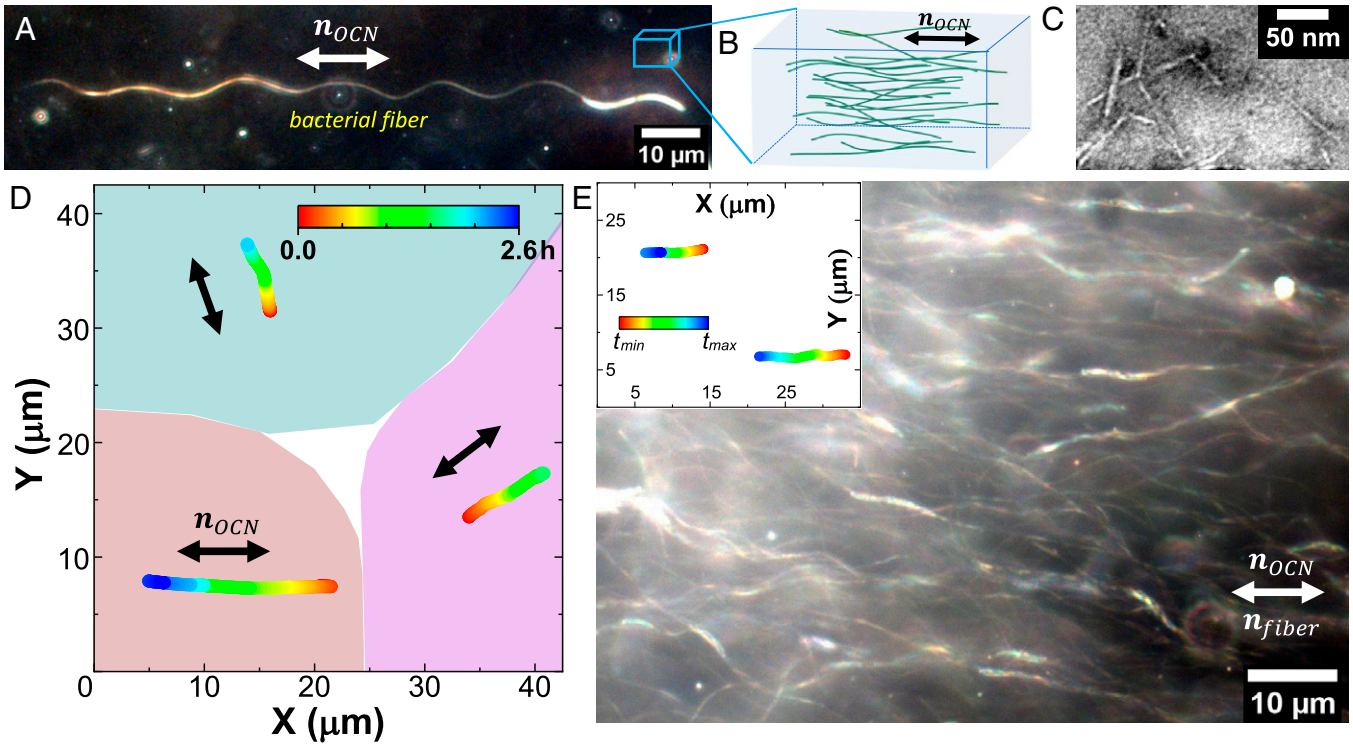

Fig. 6. Active nematics of *A. xylinum* in a colloidal fluid host of OCNs. (*A*) Dark-field microscopy image of the typical spiral-like fiber synthesized by a bacterium in the nematic fluid formed by OCNs (40). The cell propulsion is parallel to the local nematic director $\mathbf{n}_{OCN}$. (*B*) A schematic illustrating the OCNs (green) when they are concentrated into the nematic phase, as in the small part of sample marked in (*A*). (*C*) Transmission electron microscopy image of OCNs, which reveals their typical dimensions: width of 5 nm and length of up to 1,000 nm. (*D*) Typical bacteria trajectories in the polydomain OCN nematic matrix, where the different domains have different local orientations of $\mathbf{n}_{OCN}$ (black double arrows). (*E*) Aligned spiral-like fibers within an isolated OCN domain. The *Inset* shows examples of the two cell trajectories propelling parallel to $\mathbf{n}_{OCN}$.

Bacteria as Active Particles in a Medium that Develops Order through Biological Activity. A fascinating aspect of our system is that the bacteria, active particles of our active matter system, modify the environment within which they swim by producing anisotropic nanocellulose matrix. To further quantify motility of *A. xylinum* in various active nematic media and experimental conditions discussed above, we have probed the mean-square displacement, $MSD = <\Delta r^2(t)> \sim t^{\alpha}$ (41), so that the nature of bacterial motility can be assessed at different stages of ordering and gel formation by analyzing the diffusion exponent α. At long times, MSDs with $\alpha \sim 2$ reveal ballistic motions for all three probed systems (Fig. 7*A*), but $\alpha < 2$ at shorter timescales for the disordered and nematic gels. This suggests the so-called caging effect, which arises due to the 3D cellulose network that hinders swimming (42). The cage size l_{cage} can be estimated from the crossover time $t_{cross} \sim 50$ s between two regimes, where the breakdown of the ballistic response takes place (Fig. 7*A*). By employing the power function fit $MSD = 4\Gamma t^{\alpha}$ (where Γ is the diffusion rate measured in $\mu m^2/s^2$) to the experimental data, we estimate the cage size $l_{cage} = (4\Gamma t^2_{cross})^{1/2} \sim 4$ μm and ~ 1 μm in disordered and nematic gels, respectively. This agrees with a typical fiber cross-link distance extracted from the optical tweezer experiments described above for the system with no CMC additive (Movie S6). Differing from active *A. xylinum* cells producing fibers to move, the passive (nonviable) bacteria (Fig. 7*B* and Movie S8) feature Brownian motion within an isotropic liquid ($\alpha = 1$), but exhibit subdiffusive behavior in the disordered and nematic hydrogels, which is due to the fiber networks that hinder thermal motions.

Following a procedure comprising water-to-ethanol solvent exchanges, previously used for naturally occurring pellicle hydrogels (25), we have dried our nematic gels using supercritical CO_2, obtaining monodomain nematic aerogels (*SI Appendix*, Fig. S3). Anisotropic optical properties of hydrogels and aerogels, quantified by birefringence Δn, are compared in Table 1, showing that the nematic order of fibers is well preserved upon the supercritical solvent drying. Furthermore, our findings suggest that the CMC additive boosts birefringence of such nematic gels when measured both before and after the drying process. Thus, the feeding-guided ordered networks of bacteria-produced cellulose fibers can be processed into an ordered organogel and aerogel forms, expanding the potential utility of these bioderived materials.

Discussion and Conclusions

Although Dervichian's notion that the LC-like organization can be associated with functions necessary for life was related primarily to molecular systems, like organization of lipids within membranes, our findings for the *A. xylinum* bacterial community system appear to be consistent with such a scenario too. These findings reveal that the active nematic fluid and hydrogel are vibrant, "living" states of the system, whereas both inability of generating orientationally ordered biofilms and the highly ordered, dense solid-like states of the same biofilm are manifestations of decreased viability (death) for the bacterial community. Our findings show how natural living processes within the bacterial community lead to the emergence of a spontaneous active nematic LC order, which can be quantitatively characterized and controlled, for example, by the CMC additives. The progression of disorder-order and fluid-gel transitions in our system eventually leads from a vibrant, living active nematic bacterial community to the decrease of its viability within a densely cross-linked, highly ordered hydrogel. The very dense nematic gel network in our experimental setting is

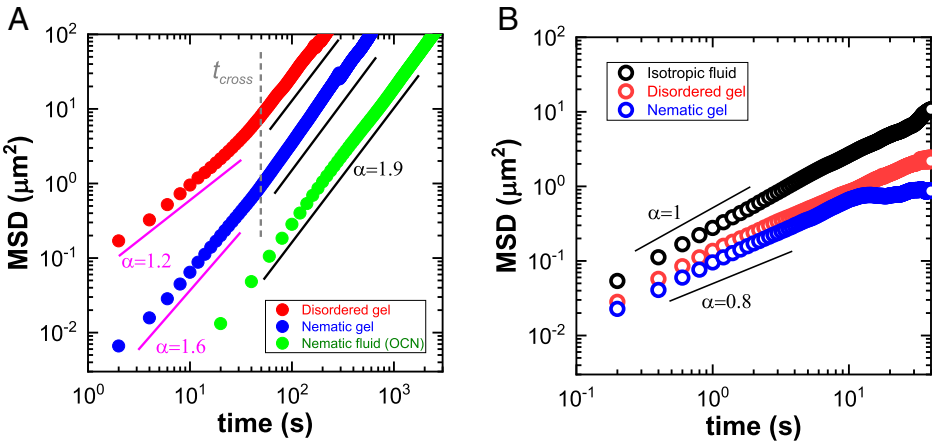

Fig. 7. MSDs of *A. xylinum* bacteria under different conditions. (*A*) Swimming *A. xylinum* cells, synthesizing nanocellulose while dispersed in the three different systems: disordered and nematic hydrogels made of bacterial cellulose and OCN nematic fluid. The MSD curves indicate a nearly ballistic regime for active nematics in OCN fluid bacterial dispersions as well as for gels at longer times above $t_{cross} \sim 50$ s (gray dashed line), with diffusion exponent $\alpha \sim 1.9$ (black solid lines). The disordered and nematic hydrogels at shorter times, however, exhibit $\alpha < 1.9$ indicative of hindered motility due to the cross-linking. The corresponding "cage" size l_{cage} of nanocellulose network is estimated to be typically 4 μm in the disordered and 1 μm in the nematic hydrogel, respectively. (*B*) MSDs of passive cells which do not produce cellulose and thus experience motion mainly due to the thermal fluctuations. Diffusion in the isotropic fluid corresponds to the Brownian motion with $\alpha = 1$. A subdiffusive regime with $\alpha < 1$ is found in both disordered and nematic hydrogels, where the particle displacements are affected by the cross-linked cellulose network.

partly a result of the confinement caused by the limited accessible volume, but the more natural conditions of such biofilms may provide means of further expansion of such nematic gels in volume without densifying them.

The ability of defining the alignment of cellulose fibers and bacteria within the active nematic LC gels by the directionality of the nutrient supply may be used not only for obtaining nematic monodomains, like described here, but also for "biopatterning such alignment," for example, by microfluidic multichannel feeding of bacterial communities. This would then be analogous to photopatterning of the LC order nowadays widely utilized for thermotropic LCs (43, 44). Such patterning of nanocellulose order within hydrogels and aerogels based on them could find technological utility in applications ranging from biological cell scaffolding to directing the flow of heat within thermally superinsulating aerogel materials derived from nematic hydrogels (25). On the other hand, the active nematic LCs studied here can serve as model systems for understanding the nature and role of biotropic phase transformations, the potential role of defects and topological solitons in defining this active nematic's behavior, including ones that can occur during the phase transformations. Our approach can potentially be used to control the disorder-to-order transition in the bacterial communities and extracellular matrices of biofilms for other bacterial systems that generate extracellular fibers and nanotubes, such as *Bacillus subtilis* nanotubes (45, 46). Furthermore, the CMC-based control of hydrogen bonding between the cellulose fibers can provide natural means of tuning physicochemical properties such as tensile strength and toughness of the ensuing hydrogels and aerogels (18, 47). Nematic LC hydrogels can be used in basic biomedical research on the artificial blood vessels (48), in tissue engineering of cartilage (49), and wound healing (50, 51). On the other hands, the dried nematic aerogels may be utilized in applications like the loudspeakers (52), food products like edible films (53), and thermal insulation (25). As bacteria-made materials with interesting properties, nematic LC gels may be also employed in green-product applications, potentially substituting plastics and other synthetic materials that are difficult to decompose or recycle after the product's life cycle.

Table 1. Birefringence of the monodomain nematic gels

CMC concentration, %	Hydrogel, $\Delta n \times 10^{-4}$	Aerogel, $\Delta n \times 10^{-4}$
0	4	1.5
1.5	7.4	15

Birefringence Δn was experimentally measured by using a microscope equipped with the Berek compensator (63). The data are provided for monodomain hydrogels and aerogels prepared without CMC additives and at the CMC concentration $c_{CMC} = 1.5\%$.

Our experiments on solid agar surfaces (Fig. 2) and direct imaging of bacterial motility in microfluidic channels upon supplying nutrients (Fig. 4) at different speeds exclude feeding-related flows or mechanical stretching as trivial sources of nematic ordering or even monodomain nature. The active LC's behavior emerges from interactions between the active particles within the cellulose producing bacterial communities, but what are the physical principles behind these interactions?

The Onsager criterion determines the critical concentration of high-aspect-ratio colloidal particles like rods needed to undergo the isotropic-to-nematic transformation (1). Hypothetically, one could imagine that the bacterial synthesis of the nanofibers continuously increases the concentration of such semirigid rods until the ensuing concentration exceeds the Onsager critical concentration (1) and, thus, could explain the underlying mechanism of nematic LC ordering in this slowly evolving system. However, our system is intrinsically out-of-equilibrium and more complex than the passive colloidal rod dispersions, though also rather different from the more conventional active matter systems studied so far (54). Notably, coupling of swimming bacteria trajectories to the directionality of the nutrient supply resembles the coupling of director of passive LCs with the external fields and the easy axes defining the surface boundary conditions. Our findings pose challenges for the development of theories capable of describing the observed disorder-to-order and fluid-to-gel transformations. While various models have been developed to describe order-disorder transitions in active matter, including two-dimensional (2D) nematic ordering of active rod-like particles (54), none of them can be directly applied to our 3D active nematic system. To quantify orderly motions of bacteria, one can qualitatively probe the 2D scalar nematic velocity order parameter φ introduced previously

for much simpler 2D systems (27, 28), obtaining $\varphi = 0.27 \pm 0.13$ and $\varphi = 0.66 \pm 0.18$ for the disordered ($\eta = 0$) and nematic ($\eta = 4$) gels, respectively (*SI Appendix*, Fig. S2 *E* and *F*). However, our active particles are bacteria with growing fibers, which can be attached to the cells producing them or not, cross-linked into a network or not. Our active matter system is 3D and with active particles that continuously morph due to bacteria growing fibers, with the emergent behavior leading to the order-disorder transition. New theoretical models are needed to gain further insights into the behavior associated with disorder-order and fluid-gel transformation of such complex, active building blocks. While the field of active matter was initiated and driven by the developments of insightful theories (54), which were then often applied to quantify and understand subsequent experimental findings, we hope that our experimental findings can now inspire new theoretical models of an active matter type that so far did not receive attention in theoretical modeling.

Future directions related to the experimental platform we have developed may include exploration of topological defects during phase transformations in such fluid and gel systems, as well as their comparison to other active nematic counterparts like the ones formed by bacteria themselves, bacteria inside lyotropic LC matrices, various nematic fluids and gels comprising microtubules, actin and kinesin motors, and so on (8, 36–39, 55–62). On the other hand, our system's close relevance to bacterial biofilms and other microbiological community systems may shed light on the physical origins of orientational ordering in various such biological systems under natural conditions.

To conclude, we have utilized cellulose-synthesizing *A. xylinum* bacteria to reveal how biological activity naturally leads to the emergence of orientational order in bacteria-made nematic fluids and gels in nutrient-rich aqueous media and atop of solid agar surfaces. Our studies revealed the monotonous increase of the scalar orientational order parameters of cellulose nanofibers and bacteria associated with fluid-gel and isotropic-nematic transformations, with the system dubbed "biotropic" in analogy with thermotropic nematics that exhibit such behavior at temperatures intermediate between the ones corresponding to crystalline solids and isotropic fluids. The nutrient supply directionality plays a role like that of confining surface rubbing and external fields in conventional LCs, enabling large-scale birefringent nematic domains with monocrystal-like order of the extracellular cellulose matrix and rod-like bacteria. We have demonstrated the means of tuning gel cross-linking density and optical anisotropy by additives like CMC, as well as that the behavior of such systems can be further controlled by using pre-existing colloidal nematics, like the ones made of charge-stabilized colloidal cellulose nanofibers. Our *A. xylinum* forms self-generating active nematic made of bacteria that move by secreting cellulose biopolymer-based nanofibers, but such studies can be extended to a variety of microbiological systems with similar types of motility. Finally, since the sources of nutrients for such bacterial communities can be various types of waste of food and beer production industry, one can envisage bioreactors converting such waste into technologically important materials like thermally insulating aerogels, ordered hydrogel scaffolding matrices for cell culturing, birefringent gels with tunable optical anisotropy, food products, and so on.

Materials and Methods

Bacteria Growth and Sample Preparation. The *A. xylinum* strain was obtained from the American Type Culture Collection (ATCC), ATCC 23769. The *A. xylinum* is a rod-shaped Gram-negative bacterium that is 0.5–1 μm wide and usually 2–10 μm long, although sometimes cells or cellular chains up to 100 μm long can be observed. The cells were kept in the freeze-dried format at −80 °C (in the Thermo Scientific Revco Ultima II Freezer) and revived according to the ATCC-prescribed protocols. The *A. xylinum* has been selected for this project as it is a model system for an efficient biosynthesis of homogeneous cellulose fibers (22). Multiple nutrition-containing media such as cotton-based waste textile (29), beer wort and food waste (25) or Standard Hestrin−Schramm (HS) media (23) can be used for the cell culture. In this work, however, we use the HS medium while following the standard protocol described in the literature (23), so that the fundamental studies we describe can be followed, reproduced and later extended by others. The used HS had pH of 6 and contained (per 1 L of water solution) 20 g glucose, 5 g vegetable peptone, 5 g yeast extract, 2.7 g sodium phosphate, and 1.5 g citric acid. Glucose was kept separately while the rest of chemicals were dissolved together. To control formation of gels, 15 g of carboxymethyl cellulose (CMC) was added into some batches to reduce the hydrogen bonding between the subfibrils. Both glucose solution and the solution of the rest of the HS's chemical composition were autoclaved for 30 min at 121 °C. Once cooled down to the room temperature, two solutions were mixed and either used immediately or stored for later at 4 °C. Agar culture plates were inoculated with *A. xylinum* and incubated for 3–4 d (*SI Appendix*, Fig. S1*A*). Single bacteria colonies were collected and dispersed in the culture tube with a 5 mL of the HS medium. The medium was then incubated for 2–3 d at 28 °C at the static conditions promoting the *A. xylinum* multiplication and cellulose fiber biosynthesis. Dense cellulose pellicles appeared as a solid floating on the liquid-air interface (*SI Appendix*, Fig. S1*C*), featuring the polydomain nematic hydrogel organization, which were collected for the optical microscopy observations (*SI Appendix*, Fig. S1 *D* and *E*).

In our experiments based on optical microscopy observations, ∼110 μL of the fluid-like diluted pellicle in the tube bulk (*SI Appendix*, Fig. S1*C*) was collected, and then injected into the so-called "μ-Slide" with I Luer Glass Bottom microfluidic channel purchased from Ibidi. This μ-Slide has a shape of rectangular prism with the following dimensions: height of either 250 μm or 450 μm, width of 0.5 cm and length of 5 cm. The μ-Slide's has two cylindrical ports (inlet and outlet) at the two channel ends, allowing for the controlled external medium exchange. The channel's outer dimensions (2.55×7.55 mm^2) allow for a facile sample integration with the used Olympus IX-81 or Olympus BX-51 microscopes, which were equipped with conventional glass slide holders. Microfluidic channel's thin-glass bottom (No. 1.5H) enables the optical microscopy observations with an inverted optical microscope while employing 60× and 100× oil immersion objectives with the numerical aperture up to 1.42. To biosynthesize the monodomain nematic cellulose at the larger scale, we used the home-made microfluidic channel (height, 1,100 μm; width, 1.5 cm; and length, 5 cm) obtained by 3D-printing with the Formlabs Form 2 resin 3D printer (purchased from Formlab). The 3D-printed channels were coassembled with thin glass slides at the top and bottom to allow for optical microscopy observations. Approximately 900 μm of highly diluted pellicles was initially injected into the home-made channel. The unidirectional feeding was applied at room temperature every 24 h by injecting 20 μL of the fresh HS medium into the inlet port of the μ-Slide by employing the PreciGenome PG-MFC Flow/Pressure Controller (*SI Appendix*, Fig. S1*F*). Simultaneously, the consumed medium was removed from the channels through the outlet port of the μ-Slide. Around 900 μL of medium was injected into the home-made channel with the same periodicity. The average flow velocity associated with feeding was 0.4 mL min^{-1} (6.7 μL s^{-1}) in all experiments reported here, though different velocities (from ∼0.003 μL s^{-1} to ∼20 μL s^{-1}) were tried in our test experiment to exclude flows as a source of ordering, with the optical microscopy observations revealing negligible contribution of the feeding flow to the bacterial motility and the ensuing network alignment. The feeding period of 24 h was chosen to avoid decline of bacterial viability caused by depleted nutrient supply (24), which has been found to occur ∼48 h after each feeding for the used dose of nutrient supply. The original motility upon sample preparation is due to glucose-based chemotaxis (33) and is polar in nature, see Fig. 4. *A–E*, and Movie S1. However, with time, as the nutrients are distributed throughout the sample by a combination of injection flows and diffusion this motility is further influenced by the preexisting oriented fibers as the

bacteria cells and linked to them fibers start moving toward the evolving nutrient-enriched regions from the nutrient depleted regions.

Following the initial injection of freely moving bacteria in a fluid-like medium into the glass cell or channel, first the dilute nematic gel/pellicle forms and then it becomes dense and gel-like over time. The initial very dilute fluid-like pellicle with few bacteria and fibers initiates the process which leads to formation of a gel with a sparse network of fibers, which then becomes more and more dense. The dense monodomain nematic hydrogel in the μ-Slide grew at room temperature under dark conditions inside the channel within typical 5–7 d after the initial injection. In the case of home-made channel, such growth took 15–20 d due to its larger volume. When the hydrogels growth saturated, the feeding was terminated, and channels ports were tightly closed with the specially designed caps to prevent the liquid media evaporation. Under such conditions, the nematic hydrogels can be stored for several months while preserving partial bacterial viability.

The used OCN colloidal dispersion was produced from the never-dried wood pulp by the TEMPO (2,2,6,6-tetramethylpiperidine-1-oxyl radical) catalyzed method (40). This chemical processing results in conversion of the secondary alcoholic group of the cellulose molecules into carboxylic acid, with the nanocellulose becoming the electrostatically stabilized colloidal nanofibers with the diameter of around 5 nm and length up to 1,000 nm. The aqueous dispersion of these nanofibers with the concentration of ∼1% possesses nematic LC properties. To study the bacteria cellulose growth and alignment in the nematic fluid host medium, the highly diluted pellicles in HS medium at $c_{CMC} = 0\%$ were collected and mixed with OCN in the ratio 1:3. The final OCN concentration in this mixture was fixed at around 0.7%. The nematic LC state of bacteria and OCN mixture was then confirmed by the birefringent texture observed in an optical polarizing microscope between crossed polarizers.

To obtain the nematic cellulose-based aerogel, the monodomain hydrogel was gently extracted from the microfluidic channel and washed in water with 1% NaOH at 80 °C for 1 h. Then, the cellulosic aerogel was immersed into an ethanol bath for 24 h for the solvent exchange. The resulting alcogel was dried to obtain an aerogel via super critical CO_2 using a Tousimis Automegasamdri 915B critical point dryer. The drying procedures are similar to the ones described in literature (25).

Optical Microscopy and Data Analysis. Experimental images and videos were captured using the phase contrast, dark-field, polarizing, and bright-field transmission-mode optical microscopy imaging modalities by employing either the Olympus IX-81 or Olympus BX-51 microscopes, as specified in figures and movies captions. These microscopes were equipped with charge-coupled device cameras Grasshopper (Point Gray Research) and dry 10×, 20×, or oil immersion 60× and 100× objectives (numerical apertures ranging from 0.3 to 1.42). The microscopes were additionally supplied with pairs of crossed linear polarizers and 530 nm full-wave phase retardation plates for the polarizing optical microscopy observations. For the dark-field imaging, we used dark-field condenser U-DCW (NA = 1.2–1.4), obtained from Olympus. For the phase contrast imaging, we employed the oil immersion 60× (NA = 1.25) objective equipped with the phase ring as well as the condenser equipped with the annular ring. The optical images of bacterial colonies were captures 2 d after their incubation on the solid agar surface. To allow for the optical observation with the high numerical aperture objectives, the colonies grown on the agar were placed onto a glass coverslip with 150-μm thickness. The videos with the active bacteria were typically recorded over the 20 min time window with the frame rate of 0.5–1 frame per second. The experimental videos were analyzed by extracting the positions of the center of mass and orientations of bacteria from each consecutive frame by employing ImageJ/FIJI's software coupled with the "wrMTrck" plugin (both are freeware products developed by the National Institutes of Health).

The video-microscopy-enabled data were exported to MATLAB for quantitative analysis. These data were used to compute the 2D scalar nematic velocity order parameter $\varphi = <\varphi(t)>_t = 2((<cos^2\chi>_t - 1/2)^2 + <sin\chi cos\chi>^2_t)^{1/2}$, where χ is the angle describing orientation of the velocity vector orientation relative to **n**, measured by analyzing video-microscopy frames (28). The mean square displacements of bacteria were quantified by using the expression $MSD(n) = (N-n)^{-1}\Sigma_i^{N-n}(\boldsymbol{r}_{i+n} - \boldsymbol{r}_i)^2$, where n is the number of a given lag time (e.g., the time elapsed between the consecutive video frames), N is total number of lag times, and $\boldsymbol{r}_i$ is the position of a given bacterium (41), respectively. To calculate the bacterial number density ρ as well as bacterial S_b and fiber S_f orientational order paraments, we acquired 30 optical images from the different sample regions 12 h after each feeding. Dark field images with 180 μm × 140 μm dimensions and phase contrast microphotographs (80 μm × 60 μm) were captured for the analysis of orientations of bacteria and fibers, respectively. The cell number density ρ was estimated by counting the cells within the images. The error bar for ρ was calculated as a population SD $s = (\sigma^2/x - 1)^{1/2}$, where σ^2 is the square of the cell number deviations on each image from the mean value, and x is the number of images. The orientation order parameters S_b and S_f were calculated through the numerical integration of particle angle distributions using the expression known for 3D nematic LCs, $S_{b,f} = 1/2 <3cos^2(\Theta_{b,f}) - 1>$ (32), where $\Theta_{b,f}$ is the angle between the bacterium's or fiber's long axis and **n**, which always emerges to be collinear with the nutrient feeding direction. The angular distributions were established by extracting ∼300 particle orientations. The error bars for S_b and S_f were calculated based on the accuracy of angular measurements using the ImageJ software. Bacteria in disordered gel appear to have slightly curved rod-like conformations, which results in the angle error measurements ±(6–8)°, contributing to the error $\Delta S_b = 0.05–0.03$ after the numerical integration. The rod-like bacterial cells in the nematic phase are more straight, thus, the angle error measurement is ±(1–3)°, yielding $\Delta S_b \sim 0.01$. In the case of cellulose fibers, the error in the orientational angle measurement is less than ±1° in both disordered and nematic gels, which is because they are thin and relatively long. Thus, the corresponding error is $\Delta S_f < 0.01$. The mean velocity of each single bacterium was calculated by dividing the path length over the elapsed time over which this path was covered while tracking cell motions with video-microscopy.

Laser Tweezers and Optical Trapping. Optical trapping and manipulations of bacteria were performed with holographic optical tweezers operating at 1,064 nm, by utilizing an Ytterbium-doped fiber laser (YLM series, IPG Photonics, maximum power of 10W) (35). The near-infrared wavelength of the tweezer's setup was chosen to assure the minimal impact of laser trapping on viability of the studied bacteria and the ensuing active nematic LCs, which is because it corresponds to the biological transparency window with minimal light absorption that could cause various side effects, like heating. This laser trapping system is integrated with the Olympus IX-81 microscope, with the beam coupled through the right-side laser port. Before entering the oil immersion 100× (NA = 1.42) objective lens used in these trapping experiments, the laser beam passes the glan-laser polarizer, a pair of plano-convex lenses, spatial light modulator, another pair of plano-convex lenses, half-waveplate, dichroic mirror, and ferroelectric polarization rotator. The laser beam power before entering the sample typically was at or below 20 mW for the bacteria in the isotropic fluid and up to 300 mW in the dense nematic hydrogel. In the latter case, the high value of power was needed due to the significant beam power loss through scattering on the cellulose network. For the microrheological experiments, the mean laser velocity was programmed to be 1.1 μm/s and 0.1 μm/s in the isotropic fluid and nematic hydrogel, respectively. The typical laser trapping forces were estimated to be around 10–20 pN. The optical manipulation experiments in the dense nematic monodomain gels were done with the nonsynthesizing *A. xylinum* cells.

Optical Anisotropy Measurements. Optical properties of various studied gels were characterized by measuring birefringence $\Delta n = n_e - n_o$, where n_e and n_o are the extraordinary and ordinary refractive indices of the monodomain nematic gels, respectively. The nematic director of both monodomain hydrogels and aerogels was oriented at 45° with respect to the crossed polarizers to provide the maximized light transmission, as well as was rotated to confirm the monodomain nature of samples via continuous rotation between the polarizers, followed by a periodic variation of light transmission. The birefringence measurements were done using the Olympus BX-51 microscope equipped with Berek compensator (63) for as-grown hydrogel samples in the home-made microfluidic channels built using two glass slides. The dry aerogel samples were also characterized for Δn when placed onto a glass slide surface. The average Δn value was determined by measuring Δn several times in different regions for each sample. The results are summarized in Table 1 for samples without and with CMC additives.

Data Availability. All study data are included in the article and/or supporting information.

ACKNOWLEDGMENTS. We acknowledge discussions with J. Cameron, E. Johnson, Q. Liu, B. Senyuk, M. Tasinkevych, and J. B. ten Hove. This research was supported by the National Science Foundation (DMR-1810513). I.I.S. also acknowledges the hospitality of the Chirality Research Center (CResCent) at the University of Hiroshima, Japan, during his sabbatical stay, where he was partly working on preparation of this article.

1. P. M. Chaikin, T. C. Lubensky, *Principles of Condensed Matter Physics* (Cambridge University Press, 2000).
2. J. Planner, Note about cholesterol. *Ann. Chem. Pharm.* **118**, 25–27 (1861).
3. F. Reinitzer, Beiträge zur Kenntniss des Cholesterins. *Monatsh. Chem.* **9**, 421–441 (1888).
4. W. J. Chung *et al.*, Biomimetic self-templating supramolecular structures. *Nature* **478**, 364–368 (2011).
5. I. I. Smalyukh, Materials science: Deft tricks with liquid crystals. *Nature* **478**, 330–331 (2011).
6. D. G. Dervichian, The control of lyotropic liquid-crystals, biological and medical implications. *Mol. Cryst. Liq. Cryst. (Phila. Pa.)* **40**, 19–31 (1977).
7. P. R. Secor *et al.*, Filamentous bacteriophage promote biofilm assembly and function. *Cell Host Microbe* **18**, 549–559 (2015).
8. I. I. Smalyukh, J. Butler, J. D. Shrout, M. R. Parsek, G. C. Wong, Elasticity-mediated nematiclike bacterial organization in model extracellular DNA matrix. *Phys. Rev. E Stat. Nonlin. Soft Matter Phys.* **78**, 030701 (2008).
9. Y. I. Yaman, E. Demir, R. Vetter, A. Kocabas, Emergence of active nematics in chaining bacterial biofilms. *Nat. Commun.* **10**, 1–9 (2019).
10. P. R. Secor *et al.*, Biofilm assembly becomes crystal clear - filamentous bacteriophage organize the *Pseudomonas aeruginosa* biofilm matrix into a liquid crystal. *Microb. Cell* **3**, 49–52 (2015).
11. R. Hartmann *et al.*, Emergence of three-dimensional order and structure in growing biofilms. *Nat. Phys.* **15**, 251–256 (2019).
12. A. K. Tarafder *et al.*, Phage liquid crystalline droplets form occlusive sheaths that encapsulate and protect infectious rod-shaped bacteria. *Proc. Natl. Acad. Sci. U.S.A.* **117**, 4724–4731 (2020).
13. G. C. Wong, Three-dimensional architecture of Vibrio cholera biofilms. *Proc. Natl. Acad. Sci. U.S.A.* **113**, 3711–3713 (2016).
14. K. Drescher *et al.*, Architectural transitions in Vibrio cholerae biofilms at single-cell resolution. *Proc. Natl. Acad. Sci. U.S.A.* **113**, E2066–E2072 (2016).
15. A. Putra *et al.*, Production of bacterial cellulose with well oriented fibril on PDMS substrate. *Polym. J.* **40**, 137–142 (2008).
16. A. Nagashima, T. Tsuji, T. Kondo, A uniaxially oriented nanofibrous cellulose scaffold from pellicles produced by Gluconacetobacter xylinus in dissolved oxygen culture. *Carbohydr. Polym.* **135**, 215–224 (2016).
17. M. M. Rahman, A. N. Netravali, Aligned bacterial cellulose arrays as "Green" nanofibers for composite materials. *ACS Macro Lett.* **5**, 1070–1074 (2016).
18. S. Wang *et al.*, Transparent, anisotropic biofilm with aligned bacterial cellulose nanofibers. *Adv. Funct. Mater.* **28**, 1707491 (2018).
19. A. Putra, A. Kakugo, H. Furukawa, J. P. Gong, Y. Osada, Tubular bacterial cellulose gel with oriented fibrils on the curved surface. *Polymer (Guildf.)* **49**, 1885–1891 (2008).
20. Q. Zhang *et al.*, Mechanical stress determines morphogenesis and cell ordering in confined bacterial biofilms. *Proc. Natl. Acad. Sci. U.S.A.* **118**, 1–8 (2021).
21. J. Nijjer *et al.*, Biofilm self-patterning: mechanical force landscaping drives a collective reorientation cascade. *arXiv:2104.08380* (11 June 2021).
22. R. M. Brown, Jr, J. H. Willison, C. L. Richardson, Cellulose biosynthesis in Acetobacter xylinum: visualization of the site of synthesis and direct measurement of the in vivo process. *Proc. Natl. Acad. Sci. U.S.A.* **73**, 4565–4569 (1976).
23. S. Hestrin, M. Schramm, Synthesis of cellulose by Acetobacter xylinum. II. Preparation of freeze-dried cells capable of polymerizing glucose to cellulose. *Biochem. J.* **58**, 345–352 (1954).
24. J. Wang, J. Tavakoli, Y. Tang, Bacterial cellulose production, properties and applications with different culture methods - A review. *Carbohydr. Polym.* **219**, 63–76 (2019).
25. B. Fleury *et al.*, Aerogel from sustainably grown bacterial cellulose pellicles as a thermally insulative film for building envelopes. *ACS Appl. Mater. Interfaces* **12**, 34115–34121 (2020).
26. N. S. Thompson, J. A. Carlson, H. M. Kaustinen, K. I. Uhlin, Tunnel structures in Acetobacter xylinum. *Int. J. Biol. Macromol.* **10**, 126–127 (1988).
27. T. Vicsek, A. Zafeiris, Collective motion. *Phys. Rep.* **517**, 71–140 (2012).
28. H. Chaté, F. Ginelli, R. Montagne, Simple model for active nematics: quasi-long-range order and giant fluctuations. *Phys. Rev. Lett.* **96**, 180602 (2006).
29. F. Hong *et al.*, Bacterial cellulose production from cotton-based waste textiles: enzymatic saccharification enhanced by ionic liquid pretreatment. *Bioresour. Technol.* **104**, 503–508 (2012).
30. T. Kondo *et al.*, Biodirected epitaxial nanodeposition of polymers on oriented macromolecular templates. *Proc. Natl. Acad. Sci. U.S.A.* **99**, 14008–14013 (2002).
31. N. Petit-Garrido *et al.*, Healing of defects at the interface of nematic liquid crystals and structured Langmuir-Blodgett monolayers. *Phys. Rev. Lett.* **107**, 177801 (2011).
32. M. Kleman, O. D. Lavrentovich, *Soft Matter Physics: An Introduction* (Springer Science & Business Media, 2007).
33. A. Basu, S. V. Vadanan, S. Lim, A novel platform for evaluating the environmental impacts on bacterial cellulose production. *Sci. Rep.* **8**, 1–8 (2018).
34. Y. Tomita, T. Kondo, Influential factors to enhance the moving rate of Acetobacter xylinum due to its nanofiber secretion on oriented templates. *Carbohydr. Polym.* **77**, 754–759 (2009).
35. R. P. Trivedi, D. Engström, I. I. Smalyukh, Optical manipulation of colloids and defect structures in anisotropic liquid crystal fluids. *J. Opt.* **13**, 044001 (2011).
36. P. C. Mushenheim, R. R. Trivedi, H. H. Tuson, D. B. Weibel, N. L. Abbott, Dynamic self-assembly of motile bacteria in liquid crystals. *Soft Matter* **10**, 88–95 (2014).
37. P. C. Mushenheim, R. R. Trivedi, D. B. Weibel, N. L. Abbott, Using liquid crystals to reveal how mechanical anisotropy changes interfacial behaviors of motile bacteria. *Biophys. J.* **107**, 255–265 (2014).
38. P. C. Mushenheim *et al.*, Effects of confinement, surface-induced orientations and strain on dynamical behaviors of bacteria in thin liquid crystalline films. *Soft Matter* **11**, 6821–6831 (2015).
39. S. Zhou, A. Sokolov, O. D. Lavrentovich, I. S. Aranson, Living liquid crystals. *Proc. Natl. Acad. Sci. U.S.A.* **111**, 1265–1270 (2014).
40. A. Isogai, T. Saito, H. Fukuzumi, TEMPO-oxidized cellulose nanofibers. *Nanoscale* **3**, 71–85 (2011).
41. X. Michalet, Mean square displacement analysis of single-particle trajectories with localization error: Brownian motion in an isotropic medium. *Phys. Rev. E Stat. Nonlin. Soft Matter Phys.* **82**, 041914 (2010).
42. E. R. Weeks, D. A. Weitz, Subdiffusion and the cage effect studied near the colloidal glass transition. *Chem. Phys.* **284**, 361–367 (2002).
43. A. Martinez, H. C. Mireles, I. I. Smalyukh, Large-area optoelastic manipulation of colloidal particles in liquid crystals using photoresponsive molecular surface monolayers. *Proc. Natl. Acad. Sci. U.S.A.* **108**, 20891–20896 (2011).
44. P. Chen, B. Y. Wei, W. Hu, Y. Q. Lu, Liquid-crystal-mediated geometric phase: from transmissive to broadband reflective planar optics. *Adv. Mater.* **32**, e1903665 (2020).
45. G. P. Dubey, S. Ben-Yehuda, Intercellular nanotubes mediate bacterial communication. *Cell J.* **144**, 590–600 (2011).
46. G. P. Dubey *et al.*, Architecture and characteristics of bacterial nanotubes. *Dev. Cell* **36**, 453–461 (2016).
47. H. Gwon *et al.*, A safe and sustainable bacterial cellulose nanofiber separator for lithium rechargeable batteries. *Proc. Natl. Acad. Sci. U.S.A.* **116**, 19288–19293 (2019).
48. D. Klemm, D. Schumann, U. Udhardt, S. Marsch, Bacterial synthesized cellulose–artificial blood vessels for microsurgery. *Prog. Polym. Sci.* **26**, 1561–1603 (2001).
49. A. Svensson *et al.*, Bacterial cellulose as a potential scaffold for tissue engineering of cartilage. *Biomaterials* **26**, 419–431 (2005).
50. M. Moniri *et al.*, Production and status of bacterial cellulose in biomedical engineering. *Nanomaterials (Basel)* **7**, 257 (2017).
51. D. Andriani, A. Y. Apriyana, M. Karina, The optimization of bacterial cellulose production and its applications: a review. *Cellulose* **27**, 6747–6766 (2020).
52. P. R. Chawla, I. B. Bajaj, S. A. Survase, R. S. Singhal, Microbial cellulose: fermentative production and applications. *Food Technol. Biotechnol.* **47**, 107–124 (2009).
53. L. Indrarti, "Incorporation of citrus essential oils into bacterial cellulose-based edible films and assessment of their physical properties" in *IOP Conference Series: Earth and Environmental Science* (IOP Publishing, Tangerang, Indonesia, 2017), pp. 012018.
54. M. R. Shaebani, A. Wysocki, R. G. Winkler, G. Gompper, H. Rieger, Computational models for active matter. *Nat. Rev. Phys.* **2**, 181–199 (2020).
55. A. Doostmohammadi, S. P. Thampi, J. M. Yeomans, Defect-mediated morphologies in growing cell colonies. *Phys. Rev. Lett.* **117**, 048102 (2016).
56. T. Sanchez, D. T. Chen, S. J. DeCamp, M. Heymann, Z. Dogic, Spontaneous motion in hierarchically assembled active matter. *Nature* **491**, 431–434 (2012).
57. F. C. Keber *et al.*, Topology and dynamics of active nematic vesicles. *Science* **345**, 1135–1139 (2014).
58. J. Berezney, B. L. Goode, S. Fraden, Z. Dogic, Extensile to contractile transition in active microtubule-actin composites generates layered asters with programmable lifetimes. *arXiv:2110.00166* (1 October 2021).
59. H. R. O. Sohn, C. D. Liu, I. I. Smalyukh, Schools of skyrmions with electrically tunable elastic interactions. *Nat. Commun.* **10**, 1–11 (2019).
60. D. Needleman, Z. Dogic, Active matter at the interface between materials science and cell biology. *Nat. Rev. Mater.* **2**, 1–14 (2017).
61. A. Doostmohammadi, J. Ignés-Mullol, J. M. Yeomans, F. Sagués, Active nematics. *Nat. Commun.* **9**, 1–13 (2018).
62. R. Zhang, A. Mozaffari, J. J. de Pablo, Autonomous materials systems from active liquid crystals. *Nat. Rev. Mater.* **6**, 437–453 (2021).
63. M. Born, E. Wolf, *Principles of Optics: Electromagnetic Theory of Propagation, Interference and Diffraction of Light* (Elsevier, 2013).